PNAS RESEARCH ARTICLE | GENETICS

Specialization of the photoreceptor transcriptome by *Srrm3*-dependent microexons is required for outer segment maintenance and vision

Ludovica Ciampi[a], Federica Mantica[a,1], Laura López-Blanch[a,1], Jon Permanyer[a,1], Cristina Rodriguez-Marín[a], Jingjing Zang[b], Damiano Cianferoni[a], Senda Jiménez-Delgado[a], Sophie Bonnal[a], Samuel Miravet-Verde[a], Verena Ruprecht[a,c], Stephan C. F. Neuhauss[b], Sandro Banfi[d,e], Sabrina Carrella[e,f], Luis Serrano[a,c,g,2], Sarah A. Head[a,2], and Manuel Irimia[a,c,g,2]

Edited by Alexander Schier, Universitat Basel, Basel, Switzerland; received September 16, 2021; accepted May 28, 2022

Retinal photoreceptors have a distinct transcriptomic profile compared to other neuronal subtypes, likely reflecting their unique cellular morphology and function in the detection of light stimuli by way of the ciliary outer segment. We discovered a layer of this molecular specialization by revealing that the vertebrate retina expresses the largest number of tissue-enriched microexons of all tissue types. A subset of these microexons is included exclusively in photoreceptor transcripts, particularly in genes involved in cilia biogenesis and vesicle-mediated transport. This microexon program is regulated by *Srrm3*, a paralog of the neural microexon regulator *Srrm4*. Despite the fact that both proteins positively regulate retina microexons in vitro, only *Srrm3* is highly expressed in mature photoreceptors. Its deletion in zebrafish results in widespread down-regulation of microexon inclusion from early developmental stages, followed by other transcriptomic alterations, severe photoreceptor defects, and blindness. These results shed light on the transcriptomic specialization and functionality of photoreceptors, uncovering unique cell type-specific roles for *Srrm3* and microexons with implications for retinal diseases.

alternative splicing | retinal disease model | zebrafish

Impaired vision is a highly heterogeneous condition affecting millions of individuals worldwide. The key feature that accounts for most visual disabilities is the primary or secondary loss of photoreceptor (PR) cells, arising from a number of different genetic and environmental causes (1). PRs, comprising rods and cones, have a unique ciliary structure named the outer segment (OS) that physically supports the phototransduction cascade, the process by which incoming light is converted into electrical signals that the brain can process (2). This ciliary function contrasts with those of other cell types, which are generally involved in sensing vibration, liquid circulation, hormones, chemicals, or temperature, and it is reflected by unique morphological characteristics. OSs are filled with densely packed and organized membranous disks that undergo rapid and extensive renewal to guarantee the proper supply of proteins, such as rhodopsin, cone opsins, and other visual pigments (3). The delivery of those components from the Golgi to the ciliary tip and back is sustained by a high-capacity vesicle-mediated transport system, carried along the ciliary axoneme (4). Consequently, multiple genes whose mutations are known to cause PR degeneration, leading to syndromic or nonsyndromic retinal ciliopathies, encode for proteins involved in OS vesicular transport (4, 5).

Alternative splicing is a pretranslational mechanism used by specialized cell types to remodel their transcriptomes to produce protein isoforms necessary for their activity. Indeed, the high degree of functional specialization of PR cells is mirrored by the unusually large fraction of genes that undergo retina-specific alternative splicing, thereby creating unique isoforms in PRs essential for different cellular properties, such as OS biogenesis (6). The unique pattern of alternative splicing in PRs has been described and is known to be at least in part driven by the action of an RNA binding protein, called Musashi 1 (*MSI1*) (7). Recently, *MSI1* expression, combined with down-regulation of the splicing factors *PTBP1* and *PCBP2*, has been linked to the activation of PR-specific exons (8). Considering that aberrant splicing due to mutations in splicing factors and retina-specific exons has been linked to several retinal diseases (e.g., retinitis pigmentosa) (9), a complete characterization of the retinal alternative splicing programs would be of great benefit for precision medicine.

Microexons are very short exons, ranging from 3 to 27 nt, that are evolutionarily conserved among vertebrates and enriched in neurons (10). These exons can encode as little as one amino acid and are often located on the surface of proteins, where they can

Significance

Retinal degeneration associated with photoreceptor death represents a major source of blindness worldwide. Photoreceptors are known to have unique functional properties, sculpted to a large extent by alternative splicing. In recent years, increasing efforts have been made to understand the intricacies of the photoreceptor-specific transcriptome, with the goal of identifying new therapeutic targets to treat retinal diseases. Here, we performed a comprehensive characterization of retinal and photoreceptor-specific microexons in vertebrates. We demonstrate that this splicing program is regulated by the splicing factor *srrm3* and that its misregulation results in severe photoreceptor alteration and visual impairment, similar to classic zebrafish models of human retinopathies. This work thus places *SRRM3* and retina-specific microexons as players in retinal health and disease.

The authors declare no competing interest.

This article is a PNAS Direct Submission.

[1]F.M., L.L.-B., and J.P. contributed equally to this work.

[2]To whom correspondence may be addressed. Email: luis.serrano@crg.eu, dibartolosa@gmail.com, or mirimia@gmail.com.

This article contains supporting information online at http://www.pnas.org/lookup/suppl/doi:10.1073/pnas.2117090119/-/DCSupplemental.

Published July 12, 2022.

modulate protein–protein interactions (10–13). The neuronal-specific Ser/Arg repetitive matrix protein 4 (*SRRM4*) controls the inclusion of most neuronal microexons annotated so far (10, 14). *SRRM4* encodes a 39-amino acid domain (enhancer of microexons, or eMIC) at its C terminus that is necessary and sufficient for the inclusion of neural microexons (14). Unlike most other neural-enriched splicing regulators (e.g., Nova or Rbfox) (15, 16), *SRRM4* is only known to act as a positive regulator through the binding of the eMIC domain to UGC motifs in the upstream intronic region near the 3′ splice sites of microexons (10). Depletion of *SRRM4* leads to neurodevelopmental defects in cell cultures as well as in in vivo models (17–20). Recently, a neurally enriched, vertebrate-specific paralog of *SRRM4*, called *SRRM3*, has been reported (14, 21, 22). *SRRM3* also encodes an eMIC domain, and both paralogs regulate a highly overlapping set of alternatively spliced small exons in vivo and in vitro (14, 21). *Srrm3* gene-trapped ($Srrm3^{gt/gt}$) mice show reduced body size and lifespan, as well as tremors and ataxia. These mice also exhibit neuronal splicing defects, which become more severe when *SRRM4* expression levels are low (21). However, the roles of *SRRM4* and *SRRM3* in PRs remain unexplored.

Here, we report that the human retina expresses the largest program of tissue-enriched microexons among all tissue types, with a subset of those included only in PRs. Retina-enriched microexons (hereafter, RetMICs) are enriched in genes involved in cilia biogenesis and vesicle transport, as well as loci known to be associated with retinal diseases. A large fraction of RetMICs and their retina-enriched regulation date back to the last common ancestor of vertebrates, suggesting a critical functional role for this program across vertebrate species. We further identify *SRRM3* as the key regulator of RetMIC inclusion in PRs. Consistently, zebrafish lacking the *srrm3* eMIC domain show progressive OS shortening, PR degeneration, and visual impairment preceded by RetMIC down-regulation from early developmental stages. Together, these results demonstrate that the conserved program of retina-specific microexons regulated by *Srrm3* is essential for PR functionality and vision, contributing to a novel understanding of retinal physiology in health and disease.

Results

The Human Retina Has the Highest Number of Tissue-Enriched Microexons. In order to systematically profile tissue-enriched microexon programs, we used data from *VastDB* (https://vastdb.crg.eu) (23) comprising 136 samples from different human cell/tissue types. For each tissue type, we aimed at identifying microexons with biased inclusion, which we defined as tissue-enriched (*Methods and Materials*). We found that the retina has the largest program of tissue-enriched microexons of all analyzed tissues (Fig. 1*A*). While this could be related to the particularly high fraction of neurons and low cell-type heterogeneity of the retina (PRs account for ∼60% of all retinal cells) (24), it could also indicate the presence of an additional set of microexons not shared with other, nonretinal neurons. Therefore, we implemented a retina specificity score to discriminate events specifically enriched in retina that takes into account the average inclusion level (using the metric "percent spliced in" or PSI) and its SD for a given exon in retinal, neuronal and nonneuronal samples (*Methods and Materials*). Using this metric, we found 75 microexons that are specifically enriched in human retinal samples (RetMICs), as well as 116 retina-enriched long exons (i.e., > 27 nt, hereafter RetLONGs) (Dataset S1). RetMICs were further subdivided into 23 microexons included exclusively in the retina (retina-exclusive) and 52 with higher inclusion in the retina compared to other neuronal samples (retina-differential) (Fig. 1*B*).

Although the mammalian retina is primarily composed of PRs, it also contains other neural cell types, such as bipolar, ganglion, horizontal, and amacrine cells. To determine whether RetMICs are mainly PR-specific, we analyzed public RNA-sequencing (RNA-seq) data from cone-rich human retinal organoids, developed from human embryonic stem cells and closely mimicking functional cones with mature OS (25). These data showed that RetMIC inclusion strongly increases during organoid development and, consequently, PR maturation (Fig. 1*C*), and shows a positive association with the expression of various PR differentiation markers (*SI Appendix*, Fig. S1 *A* and *B*). Moreover, reanalysis of an RNA-seq dataset of retinae from *Aipl1* knockout (KO) mice, which leads to specific PR degeneration (7), revealed that the vast majority (73.5%) of mouse RetMICs (see below) exhibit a substantial reduction of inclusion ($\Delta PSI < -15$) in *Aipl1* KO mice retina compared to the control (Fig. 1*D* and *SI Appendix*, Fig. S1*C*). This contrasts with neural-enriched microexons, which did not significantly change their inclusion patterns (Fig. 1*E* and *SI Appendix*, Fig. S1*D*). RetMICs also had no or low inclusion in mouse hippocampal neurons, further supporting their PR enrichment (Fig. 1*D* and *SI Appendix*, Fig. S1*C*).

Human RetMICs Are Enriched in Cilia-Related Genes and Associated with Retinal Diseases. Gene ontology (GO) analysis revealed that genes containing RetMICs are enriched for functions important for PR homeostasis, such as cilium assembly and vesicle-mediated intracellular transport (Fig. 1*F* and Dataset S2). We identified RetMIC-containing genes that localize to the cilia basal body and transition zone (*POC1B*, *ARL6*, *CC2D2A*) (26–28), where they control ciliogenesis and vesicle anchoring to the OS microtubule axoneme (Fig. 1*G*). Others regulate OS disks morphogenesis (*PROM1*) (29), PR homeostasis (*IMPDH1*) (30), are involved in anterograde and retrograde transport (*IFT88*, *DYNC2H1*, *KIF1B*) (31, 32), or are part of the centrosomal complex (*RPGRIP1L*) (33) (Fig. 1*G*). This contrasts with the GO analysis for genes harboring neural-enriched microexons, which were also enriched in functions related to vesicle-mediated transport and neural development, but not to cilia biogenesis (Dataset S2). Remarkably, RetMIC-containing genes were significantly enriched among loci associated with multiple retinal diseases (Fig. 1*H* and Dataset S3)—including retinitis pigmentosa, cone-rod dystrophies, and Bardet-Biedl syndrome—pointing to a potential role for RetMICs in vision. In line with this hypothesis, at least two individual RetMICs have been previously linked to visual impairment [*arl6* (34) and *DYNC2H1* (35)].

RetMICs Generate Alternative Protein Isoforms with Remodeled Structures. Similar to neural microexons (10), we found that RetMICs were less likely to disrupt open reading frames than RetLONGs and other cassette exons (Fig. 1*I*). Moreover, a larger fraction of RetMICs overlapped annotated PFAM or PROSITE protein domains (36, 37) (46% of RetMICs vs. 35% of RetLONGs) (Dataset S4). Together, these observations suggest that RetMICs may serve to modulate the activity of protein domains and protein–protein interactions, rather than affecting gene expression through nonsense-mediated decay or by causing gross alterations to protein folding. To perform a more comprehensive analysis of the structural impact of RetMIC inclusion, we compiled and examined all available

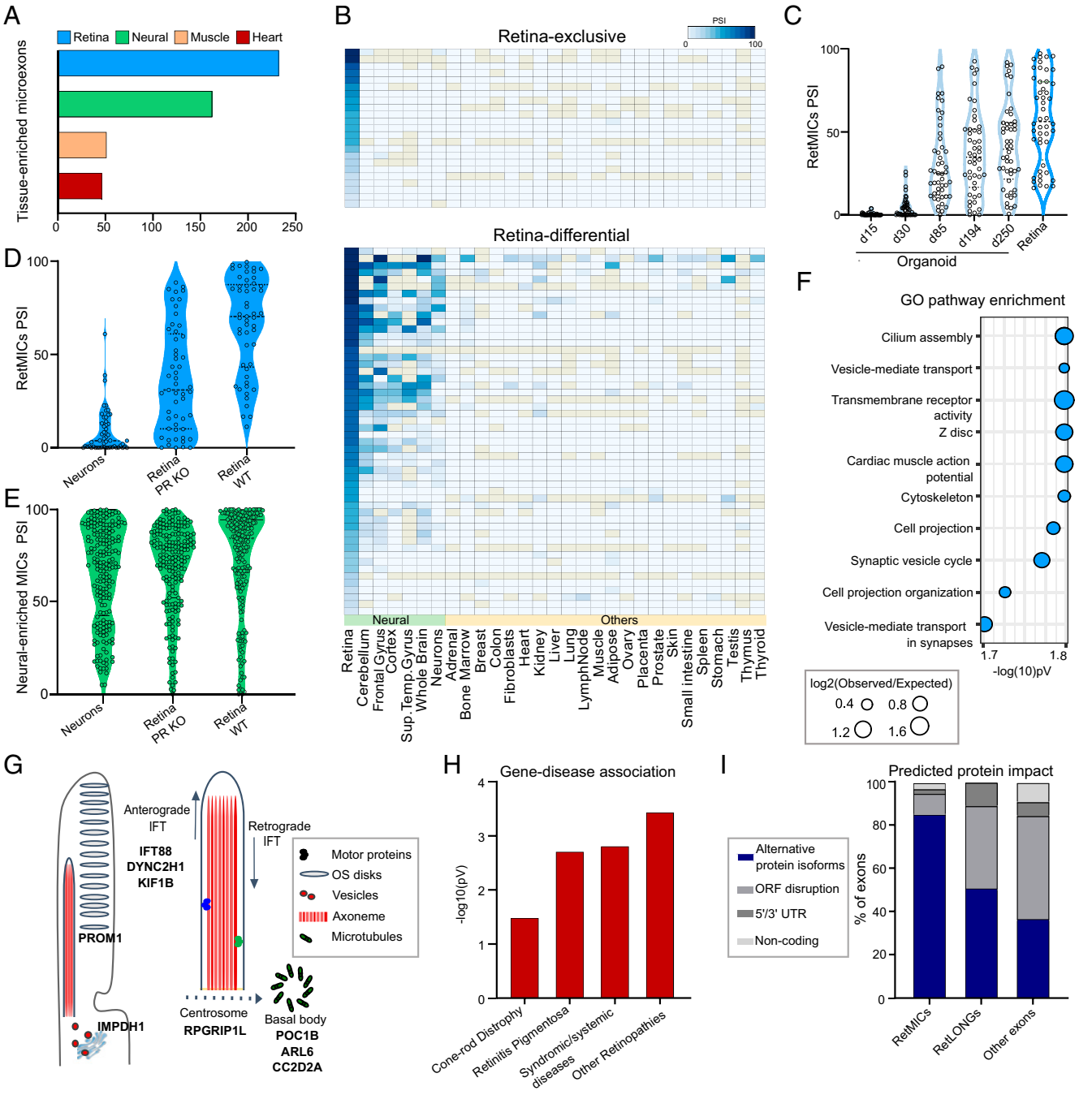

Fig. 1. Characterization and identification of the human RetMIC program. (*A*) Number of tissue-enriched microexons by tissue type in humans. Only the four tissues with the highest number of tissue-enriched microexons are depicted. (*B*) Heatmap showing RetMIC inclusion in different human tissues. RetMICs are divided into retina-exclusive (inclusion only in retina samples) and retina-enriched (biased inclusion in retina compared to neural samples). Each row corresponds to a different microexon. Inclusion levels were obtained from *VastDB* (23). (*C*) Inclusion levels (PSIs) of RetMICs in cone-rich human organoids (SRP056957) and whole retina. Developing organoid time points: day 15 (d15), day 30 (d30), day 85 (d85), day 194 (d194), and day 250 (d250). Data plotted are averaged PSIs of three biological replicates; events with NA values due to insufficient read coverage were omitted. (*D* and *E*) Violin plots depicting inclusion levels of mouse RetMICs (*D*) and neural-enriched microexons (neural MICs) (*E*) in hippocampal neurons, WT and *Aipl1* KO retinae (data from SRP068974). Events with insufficient read coverage were omitted. (*F*) Top 10 enriched GO terms for human RetMIC-containing genes. *P* values are false-discovery rate (FDR)-adjusted. (*G*) Schematic representation of the OS and localization of selected RetMIC genes; IFT, intraflagellar transport. (*H*) Enrichment of RetMIC-containing genes among loci associated with different retinal diseases. *P* values from hypergeometric tests. Complete inputs and results are provided in Dataset S3. (*I*) Predicted protein impact of different exon types as annotated in *VastDB*.

PDB structures of human RetMIC-containing genes, as well as high-confidence structural models from ModBase (38) and Interactome3D (39) (*SI Appendix*, Fig. S2 and Dataset S5). Of 32 protein structures containing the microexon insertion site, the vast majority (96%) of those sites occurred in solvent accessible regions, namely regions with relative solvent accessibility ≥20% (40). Most insertion sites were mapped to unstructured loops (72%) rather than within structured helices (20%), sheets (4%), or turns (4%), further suggesting that RetMICs generally serve to modify protein surfaces instead of impacting overall protein folding.

Through our structural analysis, we identified interesting examples of RetMICs in ubiquitous vesicular trafficking-related proteins that are likely to affect their functionality. For example,

a highly retina-specific and evolutionarily conserved 3-nt microexon (VastID: HsaEX0015816) is present in the clathrin heavy chain (*CLTC*) gene, a key protein in charge of packaging cargo into clathrin-coated vesicles at the plasma membrane (*SI Appendix*, Fig. S3 *A* and *B*). This RetMIC occurs within the N-terminal β-propeller domain, which mediates interactions with multiple clathrin-box motif-containing adapter proteins that compete for binding to the same surface (41). Upon inclusion, the microexon introduces a single negatively charged aspartic acid residue into the otherwise hydrophobic clathrin-box binding groove of the β-propeller, thereby modifying the electrostatic landscape of this interaction surface and likely affecting its interaction with adapters (*SI Appendix*, Fig. S3 *C–E*). Another interesting example is the motor protein myosin-VI (*MYO6*), which colocalizes with clathrin-coated vesicles and plays important roles in ciliary vesicular transport (42). *MYO6* harbors a conserved 9-nt retina-enriched microexon (VastID: HsaEX0041235) in the catalytic motor domain, through which myosin binds to and catalyzes movement along the actin filament through its ATPase activity (*SI Appendix*, Fig S4 *A* and *B*). The microexon is located within a loop termed "insert-1" that is not shared with other myosins and has been shown to modulate nucleotide binding (*SI Appendix*, Fig. S4 *C* and *D*) (43). This insert is thought to explain some of the unique kinetic properties of myosin-VI relative to other myosins, which may be further fine-tuned in PRs by the inclusion of the RetMIC, especially given its highly acidic sequence (Glu-Asp-Glu) that might affect the binding of negatively charged ATP. Another recent study identified a retina-enriched microexon (VastID: HsaEX0021304) within a different motor protein, dynein cytoplasmic 2 heavy chain 1 (*DYNC2H1*), which, from its position within an ATP-binding domain, also appears likely to affect conformational dynamics during microtubule binding and ATP hydrolysis (44).

RetMICs Are Evolutionarily Conserved and Enriched in Cilia-Related Genes in Vertebrates. To investigate the evolutionary conservation of RetMICs across vertebrate species, we used publicly available RNA-seq samples for mouse, chicken, and zebrafish (23), as well as zebrafish adult retina samples that we generated for this study. Similar to humans, retina was the tissue with the largest tissue-enriched microexon program in all species (Fig. 2*A*). Applying the retina specificity score to define RetMICs in mouse, chicken, and zebrafish, we identified 63 mouse, 75 chicken, and 72 zebrafish RetMICs (Dataset S1). As in mammals, zebrafish RetMICs were highly PR-specific, as shown by RNA-seq comparisons between FACS-sorted PRs and non-PR neurons (*SI Appendix*, Fig. S5). To evaluate RetMIC conservation from both the genomic and regulatory perspective, we first derived exon orthologies among all selected vertebrate species using *ExOrthist* (45) (*SI Appendix*, *Methods*). RetMICs showed significantly higher levels of genomic conservation compared to RetLONGs (Fig. 2*B*), with 84%, 62%, and 42% of human RetMICs conserved in mouse, chicken, and zebrafish, respectively. To evaluate regulatory conservation, we next investigated if genomically conserved RetMICs had retina-enriched inclusion. Preferential inclusion in the retina compared to the other tissues was observed for the majority of the human RetMIC orthologs (Fig. 2*C*), with few exceptions represented by exons characterized by broader, neural-enriched inclusion (Fig. 2*C* and *SI Appendix*, Fig. S6*A*). Overall, these results suggest an ancestral role of the RetMIC program in the vertebrate retina. To assess whether RetMICs impact similar biological processes across vertebrates, we then performed comparative GO enrichment analyses. To avoid biases coming from the different genome annotations, we transferred human GO annotations to the mouse, chicken, and zebrafish gene orthologs (*SI Appendix*, *Methods*). As for humans, cilium organization and vesicle transport appeared as enriched categories across the studied species (Fig. 2*D*), in contrast to RetLONGs (*SI Appendix*, Fig. S6*B* and Dataset S2). In summary, these results show that a program of RetMICs modulating PR ciliogenesis and vesicle transport was likely already present in the last common ancestor of jawed vertebrates.

***SRRM3* and *SRRM4* Regulate RetMIC Inclusion In Vitro.** We next looked into the regulation of RetMICs. First, we focused on *MSI1*, a splicing factor that is highly expressed in PRs and can promote the inclusion of retina-enriched exons through direct binding to UAG motifs in their downstream introns (7). However, stable ectopic expression of *MSI1* for 24 h in HEK293 cells (*SI Appendix*, Fig. S7*A*) revealed that RetMICs were largely not responsive to this regulator (Fig. 3 *A* and *B*), in contrast to some RetLONGs and known *MSI1* targets (Fig. 3*B*). Next, we tested the effect of *SRRM3* and *SRRM4* ectopic expression (*SI Appendix*, Fig. S7 *B* and *C*). Similar to neural-enriched exons (10, 14), expression of either gene was sufficient to promote the inclusion of most RetMICs (Fig. 3 *A* and *B*). Similar results were obtained using previously published data from ectopic expression of *MSI1* and *SRRM3/4* in different neural and nonneural cell lines (8, 46). Altogether, 71% of human RetMICs responded substantially (ΔPSI $\geq$ 15) to *SRRM3/4* expression in at least one experiment, in contrast to 9% for *MSI1* (Dataset S6). Moreover, *SRRM3/4* and *MSI1* showed the opposite exon length preference: whereas *SRRM3/4* enhanced mostly short retina-specific exons, *MSI1* regulated a larger fraction of long exons than of short exons (Fig. 3*C*). Analysis of the surrounding intronic sequences revealed a significant enrichment of *SRRM3/4*-binding UGC motifs upstream of RetMICs and, to a lesser extent, of short (28 to 50 nt) RetLONGs, as compared to longer RetLONGs or a set of random control exons (Fig. 3*D* and *SI Appendix*, Fig. S8*A*). In contrast, both RetMICs and RetLONGs were enriched for *MSI1*-binding UAG motifs in the downstream intron compared to control exons (Fig. 3*D* and *SI Appendix*, Fig. S8*B*). Taken together, these results suggest that *SRRM3/4* activity is sufficient to promote the inclusion of the majority of RetMICs, although *MSI1* may be able to further modulate their inclusion levels. Interestingly, we also found a significant enrichment for known binding motifs for the neural-enriched factors Nova, Rbfox, and Elavl in the upstream introns of RetMICs (*SI Appendix*, Fig. S8 *C–E*), where their binding is expected to cause exon down-regulation (47). This is in contrast with neural microexons, which showed enrichment for inclusion-enhancing Nova and Rbfox binding motifs in the downstream introns (*SI Appendix*, Fig. S8 *C–E*), as previously reported (11, 48). These neuronal-enriched splicing factors are known to have very low expression in PRs (*SI Appendix*, Fig. S8*F*) (49, 50), suggesting a differential role for these proteins in the regulation of RetMICs and neural microexons.

***srrm3* Is Necessary for RetMIC Inclusion in Zebrafish.** Unlike in most other types of neurons, *Srrm4* has been shown to be lowly expressed in adult PRs (7). Indeed, analysis of *Srrm4* expression in mouse developing rods revealed a sharp down-regulation of its mRNA levels over time (Fig. 3*E*). Interestingly, *Srrm3* displays the opposite pattern, with increasing expression during PR maturation (Fig. 3*E*). This switch in expression from *Srrm4* to *Srrm3* in mature PRs suggests that, while both *Srrm4* and *Srrm3* can induce RetMICs inclusion in vitro, *Srrm3* may

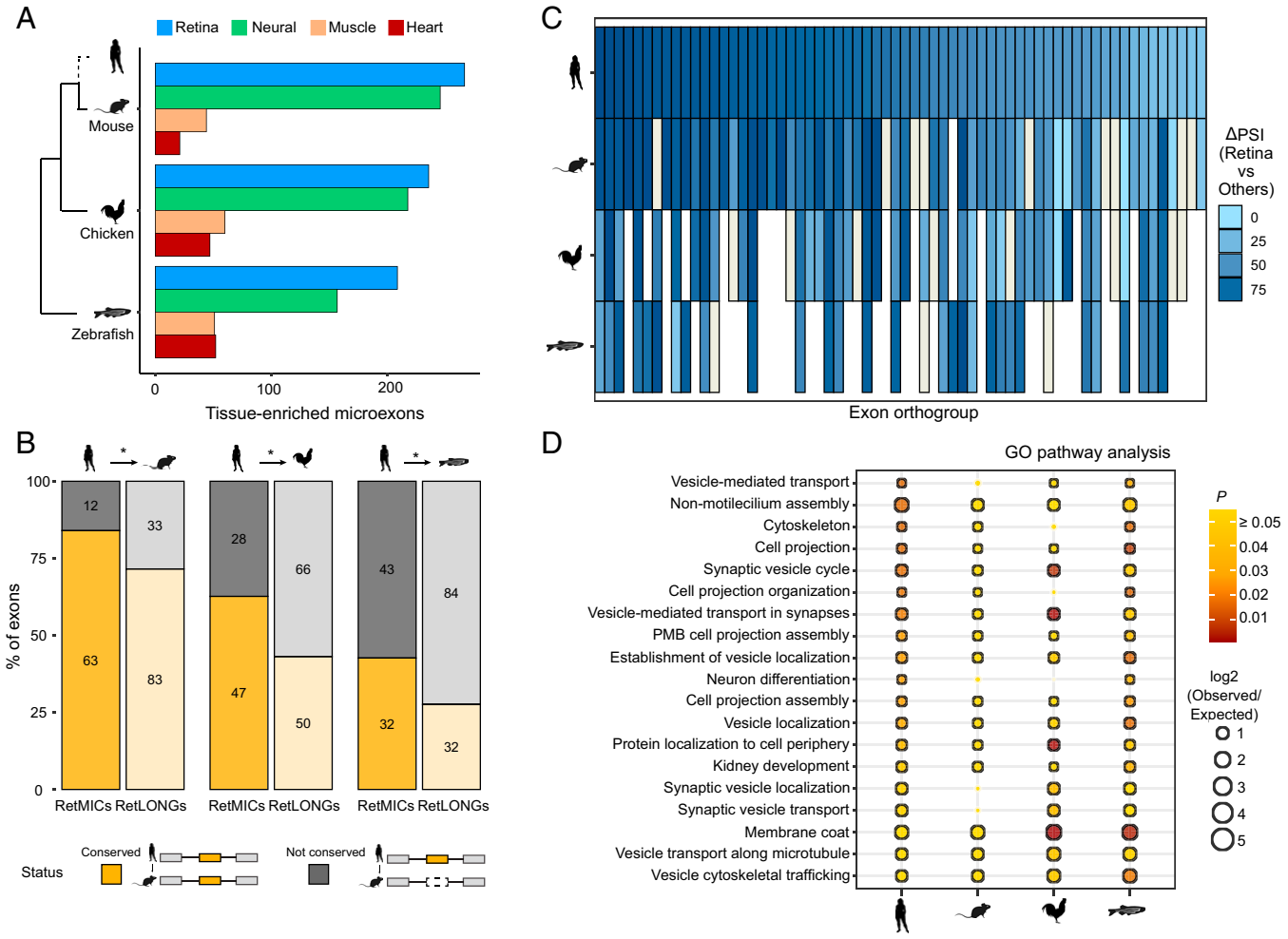

Fig. 2. Evolutionary study of RetMICs. (*A*) Number of tissue-enriched microexons (as in Fig. 1*A*) in mouse, chicken, and zebrafish. Only the four tissues with the highest number of tissue-enriched microexons are represented. (*B*) Genomic conservation of human RetMICs (full color, left bar) and human RetLONGs (transparent color, right bar) in mouse, chicken, and zebrafish. Human RetMICs/RetLONGs are considered genomically conserved in another species when they belong to an exon orthogroup including at least one exon from that species. Asterisks indicate significant differences between RetMICs and RetLONGs conservation ($P < 0.05$, hypergeometric test). (*C*) Heatmap showing the bias in retina inclusion for genomically conserved human RetMICs (top row) and their respective orthologs in mouse, chicken, and zebrafish. Each column corresponds to a different RetMIC, and the color represents the ΔPSI between the average of the retina samples and of all the other tissues, with darker blue reflecting greater retina inclusion bias. In case of multiple orthologs, only the one with the highest ΔPSI (retina − others) was plotted. Blanks and ivory rectangles indicate missing orthologs and missing ΔPSI values due to lack of read coverage, respectively. (*D*) Dot plot representing functional enrichment of RetMIC-containing genes across species. The functional enrichment of genes containing RetMICs was separately tested for each of the species, and significant categories in at least two species (FDR-adjusted $P \leq 0.05$) were plotted. The color reflects the adjusted *P* value, with yellow color depicting $P \geq 0.05$. The size of the dots is proportional to the $\log_2$ of the observed vs. expected ratio (O/E), and black borders around the categories highlight $\log_2$ O/E ≥ 1. PMD, plasma membrane bounded.

be primarily responsible for RetMIC inclusion in mature PRs in vivo. To evaluate this possibility and investigate the physiological roles of these regulators and their targets, we used the CRISPR/Cas9 system to generate zebrafish mutant lines for *srrm3* and *srrm4* by targeting the eMIC domain (14) (*Methods and Materials* and *SI Appendix*, Fig. S9 *A* and *B*). To probe the functional impact of the *srrm3* and *srrm4* mutations that we generated, we overexpressed the mutated and WT zebrafish sequences in human HEK293 cells and assessed their ability to drive ectopic microexon inclusion (14). As predicted, in contrast to the WT versions, the mutated *srrm3* and *srrm4* proteins failed to promote the inclusion of all tested microexons (*SI Appendix*, Fig. S9*C*).

While fish homozygous for the *srrm4* mutation (*srrm4* MUT) did not display any evident phenotype, including changes in size or survival rate, *srrm3* MUT and double homozygous mutant (DMUT) larvae died between 10 and 15 days postfertilization (dpf) (Fig. 4*A*). We hypothesized that this early mortality was linked to visual impairment, as reported for other zebrafish models of blindness in which the mutant fish are unable to forage for food and die of starvation after exhaustion of the yolk sac around the same days of development (51). If this were the case, we would expect that, in dark conditions, all genotypes resulting from a heterozygous (HET) cross would be equally affected, resulting in genotype ratios consistent with the Mendelian expectation. In line with this, in contrast to the specific depletion of homozygous mutants observed in control light conditions, the fish that survived at 13 dpf in the dark showed no homozygous depletion (26% WT, 39% HET, and 35% MUT) (Fig. 4*B*). These results thus indicate that, whereas all genotypes are equally likely to die in darkness, only MUT fish are more likely to do so in light conditions, pointing to a visual impairment upon *srrm3* depletion. Therefore, to directly monitor visual performance, we performed an optokinetic response (OKR) test at 10 dpf, which measures reflexive eye movements elicited by a rotating visual pattern, confirming that *srrm3* MUT fish display a severe decrease in visual performance compared to WT siblings (*SI Appendix*, Fig. S10 and Dataset S7).

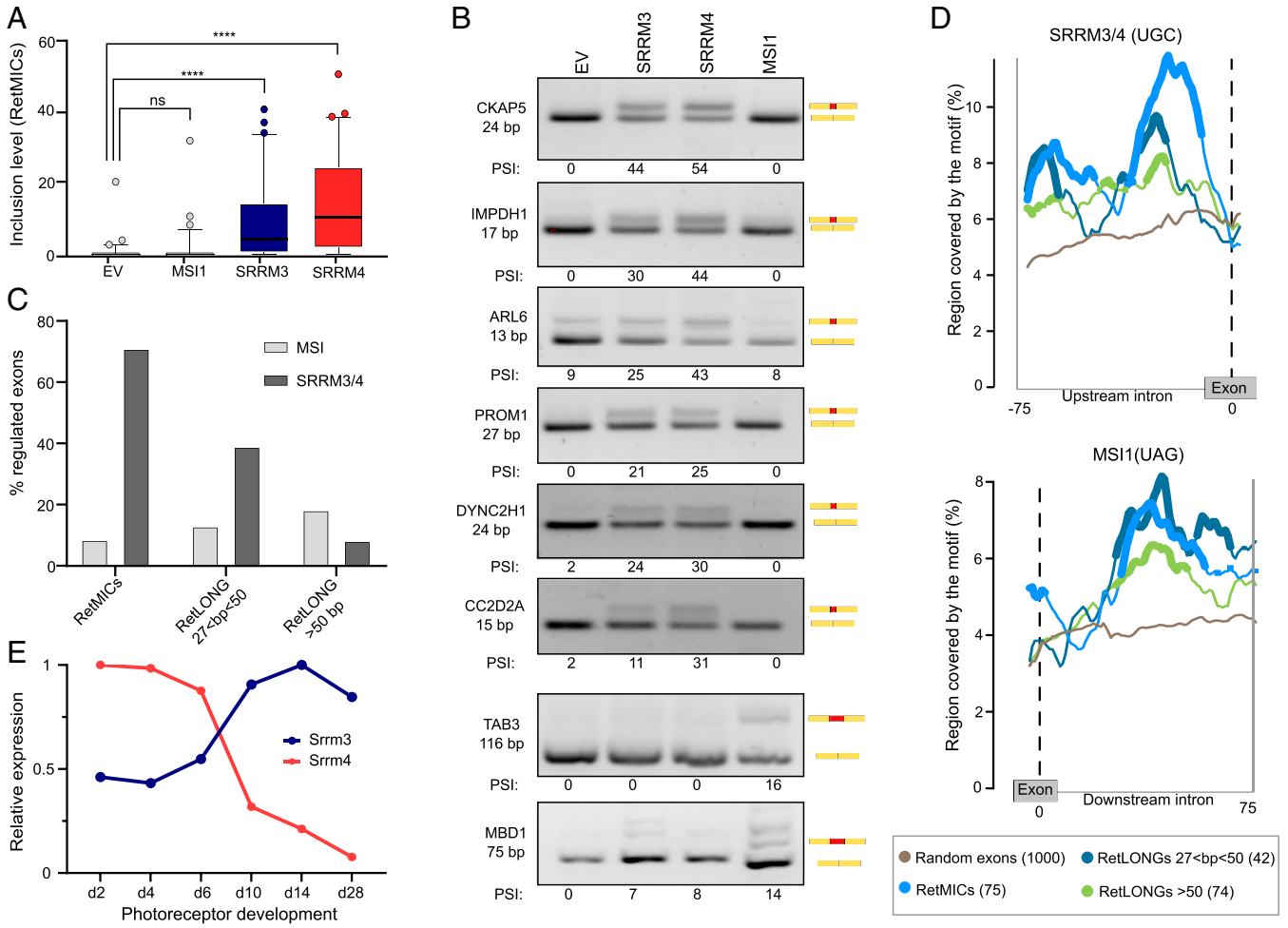

Fig. 3. Regulation of RetMICs by *MSI1*, *SRRM3*, and *SRRM4*. (*A*) Inclusion levels (using the PSI metric) of RetMICs in HEK293 cells ectopically expressing *SRRM3*, *SRRM4*, and *MSI1*. EV, empty vector. PSIs are quantified using *vast-tools* on RNA-seq data from cells 24 h postinduction with 1 μg/mL doxycycline; ****P < 0.0001 Wilcoxon test; ns: not significant. (*B*) RT-PCR assays showing the inclusion of RetMICs (*CKAP5*, *ARL6*, *IMPDH1*, *PROM1*, *DYNC2H1*, and *CC2D2A*), a RetLONG (*MBD1*), and a known MSI1-dependent exon (*TAB3*) in HEK293 cell lines upon ectopic expression of *SRRM3*, *SRRM4*, and *MSI1*. PSI levels quantified using ImageJ are shown below each gel. (*C*) Percent of retina-enriched exons by length group that showed substantial up-regulation (ΔPSI > 15) upon *SRRM3/4* (dark gray) or *MSI1* (gray) expression in at least one experiment. (*D*) RNA maps of SRRM3/4 and MSI1 associated binding motifs in the regions surrounding retina-enriched exons by length group and 1,000 random exons used as a control set. For simplicity, only the relevant upstream (SRRM3/4) or downstream (MSI1) introns are shown (full maps shown in *SI Appendix*, Fig. S8). Regions with a significant difference (FDR < 0.05) in motif coverage in the tested exon group with respect to the random exons are marked by thicker lines. Sliding window = 27 bp. (*E*) *Srrm3* and *Srrm4* gene expression levels (using the cRPKM metric) across mouse developing rods (data from VastDB). Expression levels are normalized to the stage with the highest cRPKM value for each gene.

To investigate the effect of the *srrm3* depletion in the retina at the molecular level, we next examined gene expression and splicing changes by enucleating the eyes of WT and *srrm3* MUT fish at 5 dpf and performing RNA-seq. Several genes crucial for PR functionality showed reduced expression in *srrm3* MUT eyes (e.g., rhodopsin: $\log_2$FC(MUT/WT) = −3.72) (Dataset S8), and GO analysis of down-regulated genes further revealed a strong enrichment for visual function and phototransduction (Fig. 4*C* and Dataset S9). Quantification of alternative splicing events using *vast-tools* revealed multiple misregulated exons, 53% (225 of 409) of which corresponded to microexons. Moreover, although both RetMICs and RetLONGs showed global down-regulation in mutant eyes (Fig. 4*D* and Dataset S10), RetMICs exhibited significantly larger decreases in inclusion levels than RetLONGs (P = 8.0e-5; Wilcoxon Rank-Sum test) (Fig. 4*E*).

***srrm3* Is Necessary for OS Maintenance and Visual Function in Zebrafish.** To follow up on these observations pointing at major visual defects, we then investigated the retinal morphology of the mutants. We performed immunostaining of frozen retinal sections of 5- and 10-dpf larvae using: 1) ZPR-3, a PR marker commonly used to stain rhodopsin in the OS (52), and 2) ZPR-1 (Arrestin3), a PR-specific antigen expressed in red and green double cones (52). ZPR-3 staining at 5 dpf revealed that OSs appear severely shortened and disorganized in *srrm3* MUT larvae, with different spots corresponding to rhodopsin mislocalization throughout the outer nuclear layer (ONL) (Fig. 5 *A*–*C* and Dataset S11). Moreover, we observed a significant decrease of the ONL thickness in mutant retinae already at 5 dpf (Fig. 5*G* and Dataset S11), a common signature of PR degeneration. Indeed, at 10 dpf only a few spots of rhodopsin were detected in the mutants, while the ONL disappeared completely (Fig. 5 *D* and *E*). ZPR-1 staining confirmed that cones also displayed disorganized OS and progressive degeneration at 5 and 10 dpf (*SI Appendix*, Fig. S11 *A*–*G* and Dataset S11). In contrast, histological examination of single *srrm4* MUT retinae revealed no morphological changes compared to WT fish (*SI Appendix*, Fig. S11 *C* and *F* and Dataset S11). The DMUT retinal phenotype at 5 dpf was similar to that of *srrm3* MUT but stronger (*SI Appendix*, Fig. S11 *H* and *I*). Beyond the ONL, at 5 dpf the *srrm3* MUT inner nuclear layer, inner plexiform layer, and ganglion cell layer displayed no thickness

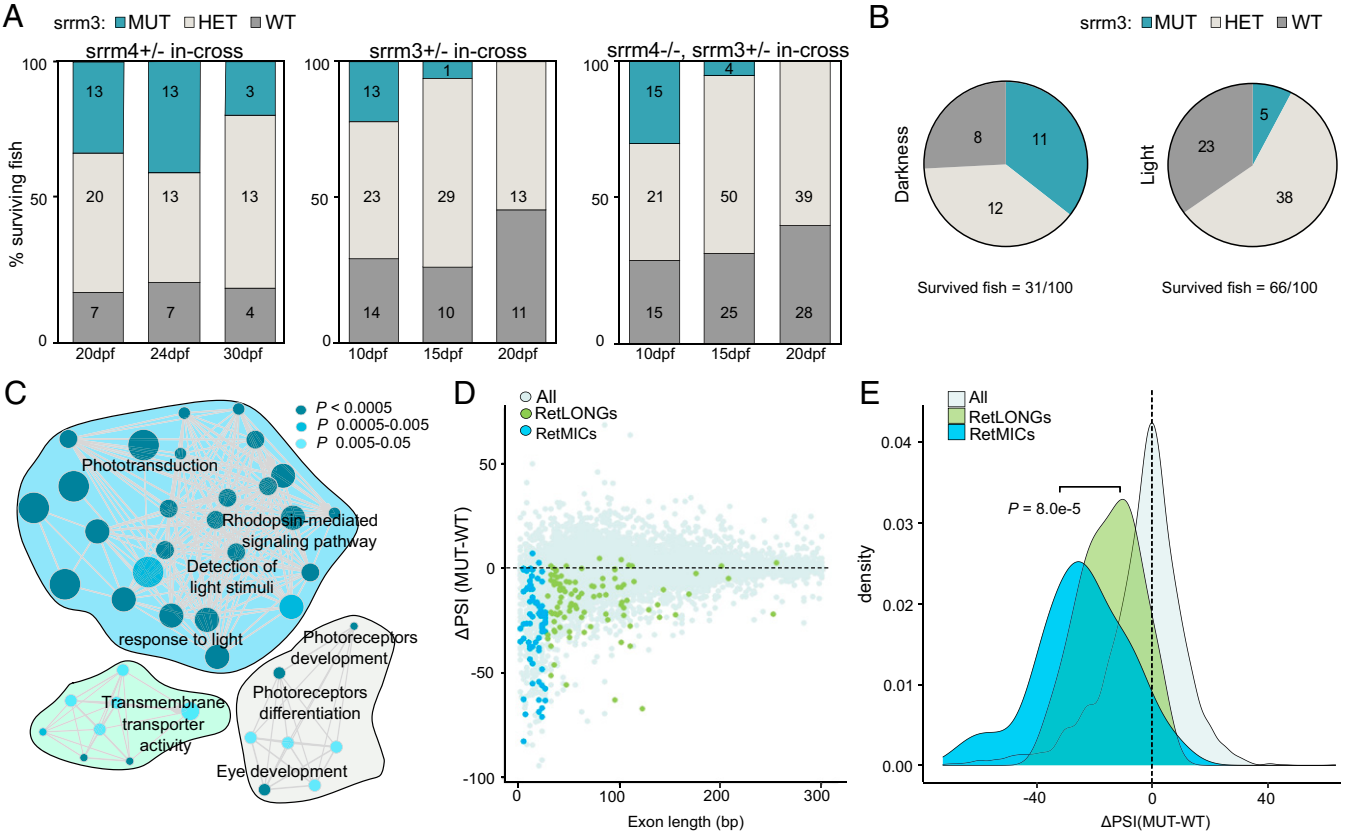

Fig. 4. *srrm3* depletion in zebrafish causes early lethality and RetMIC down-regulation. (*A*) Genotype distribution for surviving larvae at different time points from in-crosses of *srrm4*$^{+/-}$, *srrm3*$^{+/-}$, or *srrm4*$^{-/-}$;*srrm3*$^{+/-}$ (double mutants) fish. (*B*) Genotype distribution for surviving larvae at 13 dpf from a *srrm3*$^{+/-}$ in-cross in dark and control light conditions. For both *A* and *B*, the number of animals per genotype and time-point is indicated in the plots. (*C*) Enriched biological process GO terms for genes down-regulated in *srrm3* homozygous mutants (MUT) eyes at 5 dpf [$\log_2$FC(MUT/WT) ≤ −1.5]. GO terms are grouped by ClueGO into three networks according to their GO groups. GO groups are highlighted using three different arbitrary colors, as listed in Dataset S9. *P* values are corrected with Bonferroni step down. (*D*) Change in inclusion levels [ΔPSI (MUT-WT)] quantified using *vast-tools* for all exons shorter than 300 bp with sufficient read coverage in WT and *srrm3* MUT eyes at 5 dpf. Blue/green dots correspond to RetMICs and RetLONGs, respectively. (*E*) Density plots for ΔPSI distributions of RetMICs, RetLONGs, and other alternative exons (10 < PSI < 90 in WT and MUT at 5 dpf) (*P* = 8.0e-5; Wilcoxon rank-sum test).

alterations compared to WT siblings, suggesting a PR-specific phenotype (Fig. 5*G* and Dataset S11). Finally, staining of Müller glial cells revealed no obvious differences in cell morphology between genotypes (*SI Appendix*, Fig. S11*J*).

We next used electron microscopy to analyze OS ultrastructure. This analysis confirmed that OSs were dramatically shortened and disorganized at 5 dpf in both *srrm3* MUT and DMUT eyes (Fig. 5 *H–J*), indicating that the ZPR-1 and ZPR-3 signals observed by immunofluorescence largely corresponded to mislocalized proteins. These results also revealed smaller mitochondria in both mutants (Fig. 5 *H–J*), with a decrease in the total mitochondria area per field with respect to WT retinae (Fig. 5*K* and Dataset S12). In particular, the mitochondria appeared more fragmented in mutant eyes, indicating an increase in the fission process (asterisks in Fig. 5 *I* and *J*, *Lower* panels), which represents an early event prior to PR cell death (53, 54). This phenotype was more severe in DMUT eyes, showing increased numbers of mitochondria, which are smaller and even more fragmented, probably due to a higher rate of fission (*SI Appendix*, Fig. S11*K* and Dataset S12). Mutant retinae also exhibited an enlargement of the interphotoreceptor space, particularly in DMUT eyes (ips in Fig. 5 *I*, *J*, and *L*, *Lower*, and Dataset S12). This interphotoreceptor space enlargement has been reported to occur due to the accumulation of extracellular vesicles (55) and is commonly observed in animal models of PR degeneration caused by alterations in ciliary trafficking (56, 57), suggesting the presence of compromised PR cells. To monitor PR cell death, we stained retinal sections from WT and *srrm3* MUT larvae at 5 dpf with an anticaspase3 (active caspase3) antibody. The number of caspase3$^+$ cells was significantly increased in MUT animals compared to WT siblings, with the signal being specifically localized to the PR layer (Fig. 5*M* and Dataset S11).

Altogether, these results point to strong defects in retinal function already at 5 dpf. To directly monitor visual performance at this stage, we did electroretinography (ERG) recordings (Dataset S13). ERG measures field potential changes of the whole retina induced by light (58), resulting in characteristic waveforms defining the neurons contributing to the response. At 5 dpf, zebrafish photoresponse is dominated by cones while rods are not mature until around 15 dpf (59). Thus, negative ERG a-wave representing photoresponse is masked by the positive b-wave, which mirrors ON-bipolar cell response (58). We observed that *srrm3* MUT fish have a striking decrease in b-wave amplitude upon light stimulation with respect to HET and WT siblings, indicating a strong visual impairment (Fig. 5*N* and *SI Appendix*, Fig. S12*A*). DMUT fish performed even worse than *srrm3* MUT fish (Fig. 5*N* and *SI Appendix*, Fig. S12*B*), supporting a minor but significant overlapping role for *srrm4*. Nevertheless, single *srrm4* MUT fish did not display any significant visual impairment compared to WT siblings (*SI Appendix*, Fig. S12 *C* and *D*).

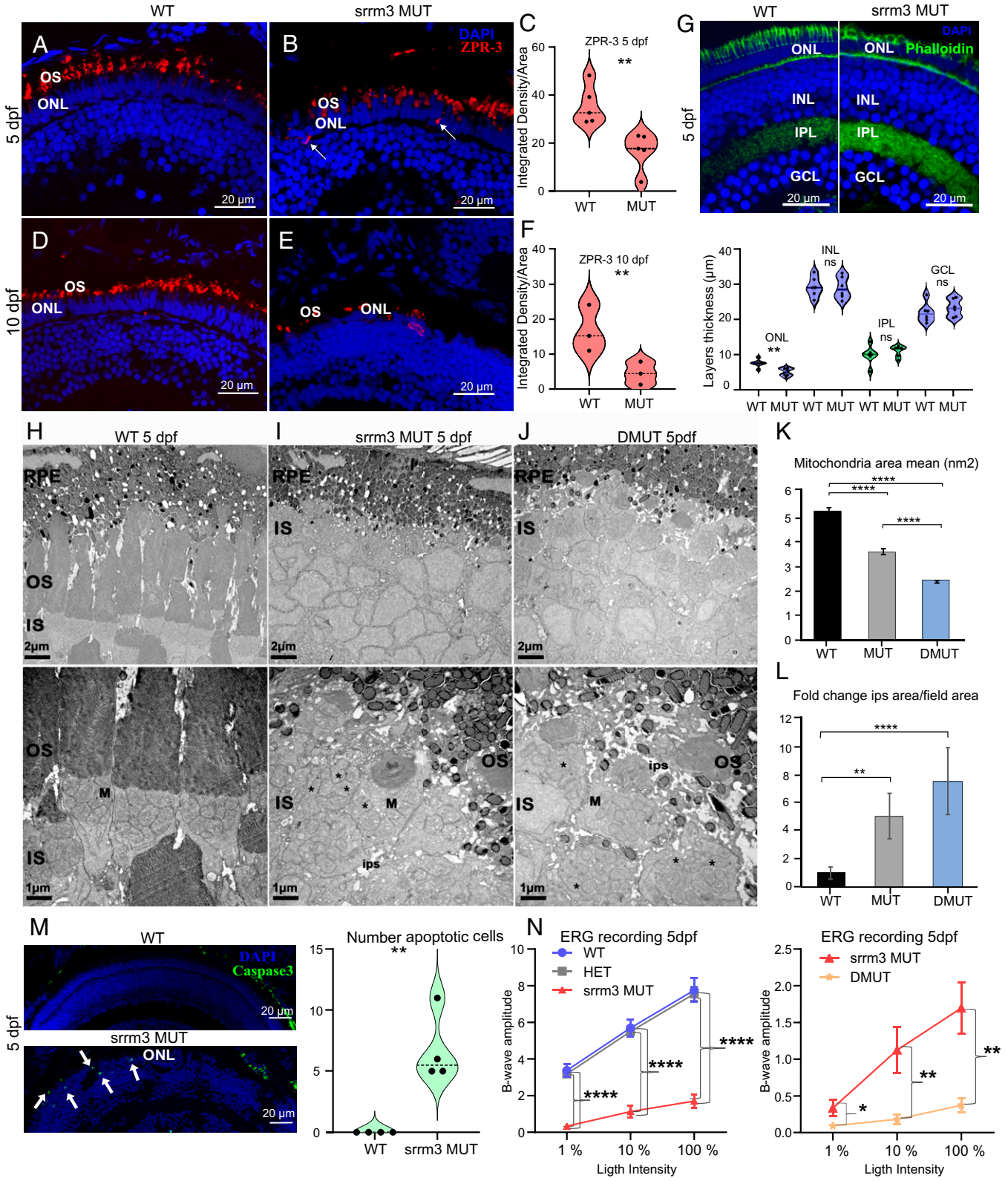

Fig. 5. PR degeneration and visual impairment in *srrm3* mutants. (*A–F*) ZPR-3 staining in WT (*A* and *D*) and *srrm3* homozygous mutants (MUT) (*B* and *E*) siblings at 5 and 10 dpf. Arrows show rhodopsin mislocalization. $n = 5$ for 5 dpf and $n = 3$ for 10 dpf fish. Quantifications of the ZPR-3$^+$ area are provided for 5 dpf (*C*) and 10 dpf (*F*). *P* values from unpaired *t* tests. (*G*) Phalloidin staining in WT and *srrm3* MUT retinae. The violin plot shows a thickness analysis for different retina layers: inner nuclear layer (INL), inner plexiform layer (IPL), and ganglion cell layer (GCL); $n = 6$. *P* values from unpaired *t* tests. (*H–J*) Electron microscopy images show absence of OSs or a dramatic OS length decrease in eyes of both *srrm3* MUT (*I*) and DMUT (*J*) compared to WT ones (*H*) at 5 dpf; $n = 2$ for all the genotypes. Further magnification in the *Lower* panels (*H–J*) revealed smaller mitochondria (asterisks indicate mitochondria in fission process) and enlarged interphotoreceptor space (ips), quantified as mean of mitochondria area per field and interphotoreceptor space area normalized on field area, represented as fold-change (FC) in *K* and *L*, respectively. *P* values from one-way ANOVA tests with Tukey post hoc analyses. (Scale bars, 2 µm, *Upper*, and 1 µm, *Lower*.) $n \geq 4$ eyes per genotype; $n \geq 13$ fields per genotype were analyzed. (*M*) Caspase3 staining and associated quantifications in 5 dpf retina sections. $n = 4$ for each genotype. (*N*) Averaged ERG b-wave amplitudes from WT, *srrm3* HET, and *srrm3* MUT, or *srrm3* MUT and DMUT at 5 dpf upon different light stimuli (1%, 10%, and 100%). All recordings were done in two independent experiments. $n = 20$ for WT, $n = 34$ for *srrm3* HET, $n = 17$ for *srrm3* MUT (*N*), $n = 22$ for *srrm3* MUT (*O*), and $n = 15$ for DMUT. *P* values from one-way ANOVA tests. Error bars correspond to the SEM. Significance code for all tests: ****$P = 0$; ***, $0 < P < 0.001$; **, $0.001 \leq P < 0.01$; *, $0.01 \leq P < 0.05$.

Early Missplicing of RetMICs Precedes PR Degeneration and Other Transcriptomic Alterations. Although *srrm3* is mainly known to regulate short exons, it is conceivable that the phenotypes observed at 5 dpf could be caused by other molecular alterations. Therefore, we investigated the onset of molecular and morphological alterations at earlier time points. First, we determined the expression dynamics of *srrm3* and *srrm4* by qPCR assays on eyes from 24 hours post fertilization (hpf) to 20 dpf larvae. Although both genes had comparable expression levels at 24 and 48 hpf, *srrm3* showed much higher expression than *srrm4* from 5 dpf onward (*SI Appendix*, Fig. S13*A*), in line with the pattern observed in mouse PRs (Fig. 3*E*). In addition, we did not observe compensatory up-regulation of *srrm4* in *srrm3* MUT eyes (*SI Appendix*, Fig. S13*B*). Second, we performed RNA-seq of WT eyes at 24, 48, 60, and 72 hpf. These data revealed that RetMICs start being progressively included from 48 to 60 hpf (Fig. 6*A* and Dataset S10), around the time when the OSs start differentiating in zebrafish (60). This inclusion pattern was further validated by RT-PCR assays for several representative RetMICs (*SI Appendix*, Fig. S13*C*).

Next, we performed RNA-seq of eyes from the corresponding *srrm3* MUT siblings at 48, 60, and 72 hpf and investigated the timing of misregulation of microexons and longer exons, as well as of gene expression (Datasets S8 and S10). Importantly, whereas more RetMIC skipping was observed in *srrm3* MUT respect WT fish as early as 48 hpf (Fig. 6*B* and *SI Appendix*, Fig. S13*C*), and it increased progressively over time up to 5 dpf (Fig. 6*B* and *SI Appendix*, Fig. S13*C*), neither RetLONGs nor retina-specific genes (RetGENEs) (*Methods and Materials*) showed global down-regulation of inclusion/expression until 5 dpf (Fig. 6*B* and Dataset S10). A similar overall pattern was observed for all microexons, long exons, and genes that were found to be down-regulated in *srrm3* MUT eyes at 5 dpf (Fig. 4 *C* and *D* and Dataset S10), among which only microexons showed a general down-regulation before 5 dpf (*SI Appendix*, Fig. S14*A* and Dataset S10). Moreover, differential

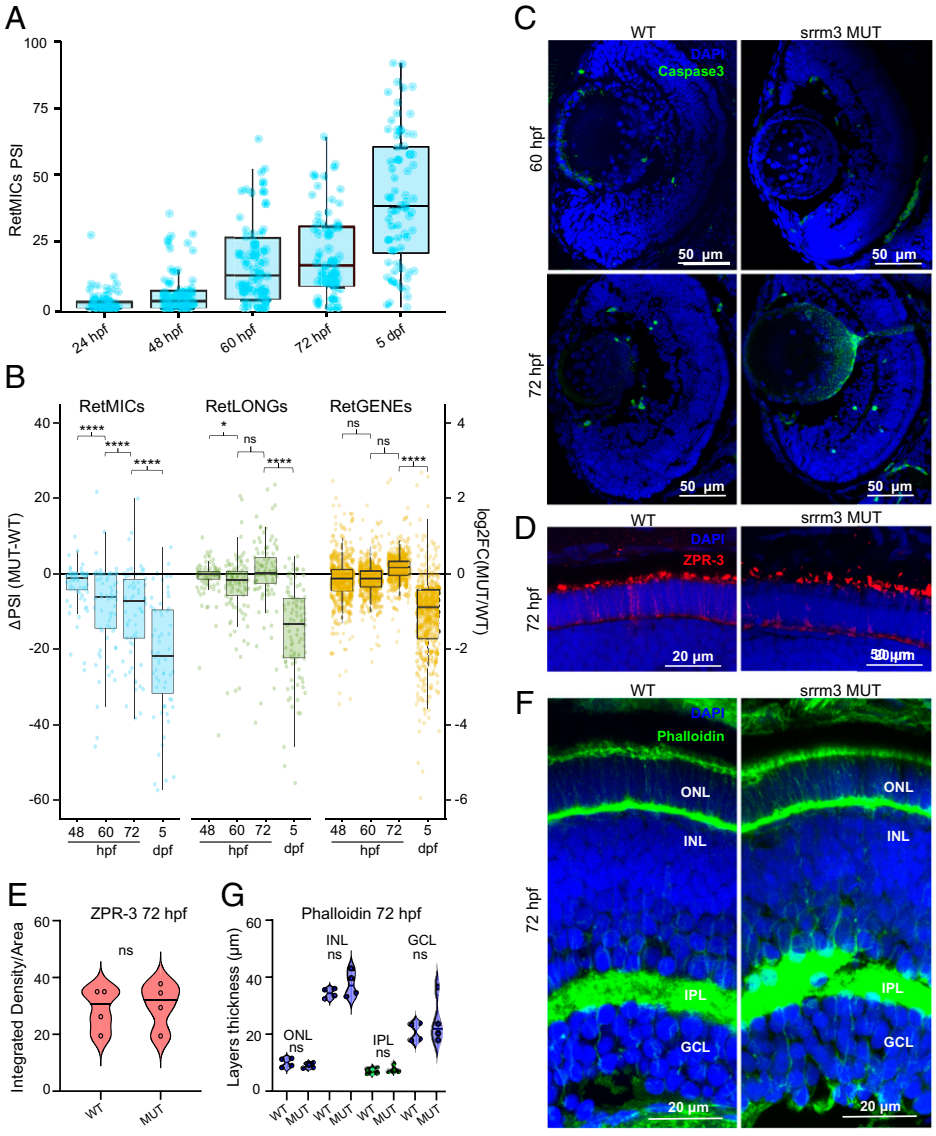

Fig. 6. Transcriptomic and morphological alterations of *srrm3* mutants throughout development. (*A*) Inclusion levels (PSIs) of RetMICs in WT zebrafish heads at 24 hpf and eyes at 48 hpf, 60 hpf, 72 hpf, and 5 dpf. (*B*) Box plots showing the distribution of changes in inclusion levels for RetMICs and RetLONGs [ΔPSI (MUT-WT)] (left *y* axis) and in expression levels for RetGENEs [$\log_2$FC(MUT/WT)] (right *y* axis) in WT and *srrm3* MUT eyes at different time points. Only exons with sufficient read coverage across all conditions are shown. *P* values from paired one-tailed Wilcoxon tests. (*C*) Caspase3 staining for WT and *srrm3* MUT retinae at 60 hpf and 72 hpf; $n = 4$ for all genotypes and conditions. (*D* and *E*) ZPR-3 staining (*D*) and positive area quantification (*E*) for WT and *srrm3* MUT retinae at 72 hpf; $n = 4$. *P* values from unpaired *t* tests. (*F* and *G*) Phalloidin staining (*F*) and thickness analysis for different retinal layers (*G*) for WT and *srrm3* MUT retinae. $n = 4$. *P* values from unpaired *t* tests.

gene-expression analyses at each time point revealed much fewer down-regulated genes [$-\log_2$FC(MUT/WT) < 1.5] in MUT eyes at 48, 60, and 72 hpf than at 5 dpf (Dataset S8), and gene set enrichment analysis (GSEA) showed no enrichment for PR-related categories among those genes (*SI Appendix*, Fig. S14*B* and Dataset S14). This pattern was confirmed through qPCR assays for some representative PR genes (*SI Appendix*, Fig. S14*C*).

These observations thus indicate that microexon misregulation precedes the broad, transcriptome-wide changes found at 5 dpf, which are likely caused indirectly by the observed PR malformations and death (Fig. 5*M*). Consistently, GSEA revealed a significant enrichment in apoptosis-related categories among up-regulated genes exclusively at 5 dpf (*SI Appendix*, Fig. S14*B*), and no apoptotic cells were detected by caspase3 staining on 60 and 72 hpf retinae (Fig. 6*C*). Moreover, we found no alterations in retinal layering or OS morphologies in *srrm3* MUT larvae compared to WT siblings at either 60 hpf (*SI Appendix*, Fig. S15) or 72 hpf (Fig. 6 *D*–*G* and Dataset S11). Finally, injection of mRNA encoding only the eMIC domain of human *SRRM3* (10, 14) into *srrm3* MUT zebrafish embryos rescued the inclusion of tested representative microexons at 5 dpf (*SI Appendix*, Fig. S16*A*) and restored PR morphology and ONL thickness, as shown by Phalloidin staining (*SI Appendix*, Fig. S16*B* and Dataset S11). Altogether, these results point to a direct and specific role of microexons in causing the described phenotypes in *srrm3* MUT zebrafish.

Discussion

Alternative splicing is an essential mechanism for generating molecular and functional diversity across cell and tissue types. In the context of the nervous system, which shows a particularly high degree of tissue-enriched alternative splicing, PRs differ in their transcriptomic profiles from other neuronal subtypes (50), likely as a reflection of their unique cellular morphology and function. Our results reveal a program of retina-enriched microexons that further contribute to this molecular specialization. These microexons are included in PRs in addition to neural microexons, which are shared with other neuronal types, and both microexosn programs have distinct and common regulatory and functional properties.

We demonstrate that the ectopic expression of either *Srrm3* or *Srrm4* is sufficient to drive the inclusion of most RetMICs in non-PR cells, as was shown for neural microexons (10, 21). However, we show that only *Srrm3* is highly expressed in mature PRs and that the inclusion of most RetMICs depends mainly on this paralog in vivo. Nevertheless, we also found evidence for a minor but significant redundant role for *srrm4* in the retina, since double mutant fish displayed stronger visual impairment and histological defects than single *srrm3* mutants. Given the substantial levels of both *Srrm3* and *Srrm4* expression in other neuronal types (17, 21), these results thus raise the question of why RetMICs, particularly the retina-exclusive ones, have low or no inclusion in non-PR neurons. At least two nonmutually exclusive hypotheses may explain this pattern. First, although we found that the PR-specific splicing factor MSI1 on its own is not sufficient to drive the inclusion of most RetMICs, it is possible that MSI1 is necessary for RetMIC splicing in PRs in vivo, acting synergistically with SRRM3. In line with this hypothesis, we found a significant enrichment for MSI1 binding motifs in the downstream introns of both RetMICs and longer retina-enriched exons, a binding location that is expected to promote exon inclusion (7). Second, we found that RetMICs, in contrast to neural microexons, have enrichment for known binding motifs of Nova, Rbfox, and Elavl families, in positions expected to repress their inclusion (47). Given that these factors have very low expression in PRs but high in other neuronal cells (49, 50), it is plausible that these splicing factors could act as negative regulators of RetMICs in non-PR neurons, allowing for their inclusion only in PRs. Further research should evaluate these hypotheses to provide a more complete mechanistic understanding of the unique inclusion profile of RetMICs promoted by *Srrm3*.

At the functional level, we found that, similar to neural microexons (10), RetMICs can remodel protein structures of genes enriched for vesicle-mediated transport and related functions. However, we also revealed an enrichment for genes involved in cilium assembly, which was not observed for neural microexons. Altogether, these functions suggest that RetMICs enable a unique proteome specialization that is necessary for proper development and functioning of the OS, the highly modified cilium of PRs. Given the unusually high demand for vesicle formation, transport, and recycling in the OS (4), the specific modifications introduced by RetMICs in otherwise ubiquitous trafficking and ciliary machinery may help meet this high demand by promoting interactions with PR-specific substrates and facilitating unique catalytic properties not required (or even detrimental) in other cell types. In line with this idea, depletion of *srrm3* caused severe malformation of the OS and vesicle accumulation, leading to PR degeneration and impaired visual function. Importantly, in homozygous *srrm3* mutant larvae, OSs are generated but not maintained. This phenotype is similar to that described for various zebrafish mutants of terminal effector genes involved in intraflagellar transport (61), where mislocalization of visual pigments is associated with OS disappearance and PR degeneration. Furthermore, mutations in other genes necessary at different stages of ciliogenesis or vesicle trafficking (29, 57, 62) result in PR phenotypic alterations characterized by vesicle accumulation and dysmorphic OSs. Remarkably, the nearly complete loss of the OS that we report for *srrm3* places this microexon regulator among the genes with the strongest mutant PR phenotypes reported so far in zebrafish, with features matching the ones observed in human retinitis pigmentosa (63).

Importantly, we show that RetMICs (as well as other microexons), but not RetLONGs or RetGENEs, were significantly dysregulated in *srrm3* mutants at early time points, before morphological alterations or increased apoptosis were observed. Moreover, we demonstrated that morphological phenotypes in PRs can be rescued solely by injection of mRNA encoding the eMIC domain into zebrafish embryos, which is specifically responsible for microexon inclusion (14). Taken together, our results suggest that microexon misregulation is, at least to a large extent, directly responsible for the phenotypes we described in *srrm3* mutant fish. However, it should be noted that, in addition to RetMICs, depletion of *srrm3* also affected the inclusion of many neural-enriched microexons and other short exons in zebrafish eyes, whose misregulation likely contributes to the observed phenotypes. Nevertheless, three additional observations support that RetMICs, in particular, are likely to be directly behind at least some of the *srrm3* mutant phenotypes. First, the inclusion of RetMICs was strongly misregulated in the eyes of *srrm3* mutants. Second, as mentioned above, misregulation or mutation of the RetMICs in *arl6* (34) and *DYNC2H1* (35), respectively, have been shown to directly impact visual function, in line with the *srrm3* mutant phenotypes observed here. Third, zebrafish lacking individual RetMIC-containing genes, such as *cc2d2a* (57) and *ift88* (61),

have been shown to display disorganization of the vesicle fusion machinery and strong PR degeneration. Therefore, and although some of the RetMICs highlighted here are in fact not strongly misregulated in *srrm3* mutants (*arl6*; $\Delta PSI = -8$) or even conserved in zebrafish (*DYNC2H1*), it is plausible that the multiple PR-related phenotypes caused by *srrm3* mutation are at least in part caused by misregulation of RetMICs in genes with PR-related functions. However, which individual RetMICs underlie the *srrm3* mutant phenotypes and through which molecular and cellular mechanisms they operate need to be further investigated. Remarkably, revealing their functional roles in PR differentiation and function would place RetMICs as candidates to underlie retinopathies without a known genetic cause, opening new avenues for the understanding of the highly complex molecular genetics of retinal diseases.

Methods and Materials

Definition of Tissue-Specific Exons and RetMICs, RetLONGs, and RetGENEs. We downloaded exon inclusions levels and associated information from *VastDB* (23) for all the species included in the manuscript (human: hg38; mouse: mm10; chicken: galGal4; zebrafish: danRer10) and employed the *Get_Tissue_Specific_AS.pl* (64) script to derive sets of tissue-enriched microexons using the config files listed in Dataset S15. Definition of RetMICs and RetLONGs was then done based on a retina specificity score that takes the distributions of retina and neural samples into account. For RetGENEs, we used a comparable approach through the *Get_Tissue_Specific_GE.pl* (64) script.

Regulatory Analysis of RetMICs and RetLONGs. HEK293 lentiviral cell lines used in this study to ectopically express *SRRM3*, *SRRM4*, or *MSI1* were generated using a previously described protocol (46). pCW57.1 lentiviral vector (empty vector) was used as a negative control. Expression of the transgenes was induced using 1 μg/mL of doxycycline for 24 h. RNA was used for RT-PCR assays (primers listed in Dataset S16) and RNA-seq (mapping statistics in Dataset S17). RNA maps were done using the *rna_maps* function from *Matt* (65) for *NOVA* (YCAY), *RBFOX* (GCATG), and *ELAVL* (TTTNTTT) binding motifs.

Generation of *srrm3* and *srrm4* Zebrafish Mutant Lines. Fish procedures were approved by the Barcelona Biomedical Research Park Institutional Animal Care and Use Ethic Committee (PRBB–IACUEC). To create zebrafish mutant lines (*SI Appendix*, Fig. S9), we used CRISPR/Cas9 to target the eMIC domain of *srrm3* [Tg(HuC:GFP; srrm3_eMIC); GGGAATAA CTGCGTGAGCGGCGG] and *srrm4* [Tg(HuC:GFP; srrm4_eMIC); TGATTCTGCGGGCTTCCAGGTGG]. Mutant sequences were probed for microexon regulatory activity by transfecting them into HEK293, as previously described (14).

Immunofluorescence and Histological Retinal Analyses. Zebrafish eyes were fixed in 4% paraformaldehyde (PFA) overnight, cryoprotected with 30% sucrose overnight, embedded in OCT, and cryosectioned. Twenty-micrometer cryosections were collected on slides. For PR marker staining, sections were incubated with primary antibodies (ZPR-1 [ZDB-ATB-081002-43] 1:400 and ZPR-3 [ZDB-ATB-081002-45] 1:200, Zebrafish International Resource Center, GS6 [Millipore]) overnight in blocking solution. Sections were then incubated with the Alexa Fluor secondary antibodies (1:1,000; Invitrogen) and counterstained with DAPI (Vector Laboratories). The Phalloidin staining was performed using a previously described protocol (66). The caspase3 assay was performed on retina sections following the protocol described above (anticaspase3; Fisher Scientific, 15889738; 1:500). Imaging analyses were done with the ImageJ tool.

Electron Microscopy. The samples were cut on ultramicrotome Leica EM UC7 and collected on the single-slot oval grids and analyzed with an FEI electron microscope. OS, mitochondrial, and interphotoreceptor space area was determined using FEI software. The analysis was carried out on four eyes per genotype, for each genotype an $n \geq 13$ fields was analyzed.

ERG and OKRs. For ERG experiments, *srrm3* MUT, *srrm4* MUT and DMUT larvae as well as different control siblings were recorded at 5 dpf, as previously described (67). OKRs were recorded as described previously (68).

Data Availability. Extended methods can be found in *SI Appendix*. RNA-seq data have been deposited in the Gene Expression Omnibus (GEO) database (accession no. GSE180781) (69). All other RNA-seq samples used in this study are publicly available and listed in Dataset S17. All other study data are included in the main text and supporting information.

ACKNOWLEDGMENTS. We thank Juan Valcárcel and Juan Ramón Martínez for scientific support and critical reading of the manuscript; Xavier Hernandez-Alias, Antonio Torres-Méndez and Alessia Indrieri for scientific discussion; Claire Lastrucci for supervision during the initial stages of the project; Xavier Henandez-Alias and Miquel Anglada-Girotto for assistance during the bioinformatic analysis; Jochen Hecht and the CRG Genomics Unit for the RNA-sequencing services; Elena Polishchuk and the Telethon Institute of Genetics and Medicine Advanced Microscopy and Imaging Facility for the Electron Microscopy services. We acknowledge the support of the Spanish Ministry of Science and Innovation through the Centro de Excelencia Severo Ochoa (CEX2020-001049-S, MCIN/AEI/10.13039/501100011033), and the Generalitat de Catalunya through the CERCA programme.

Author affiliations: [a]Centre for Genomic Regulation, Barcelona Institute of Science and Technology, 08036 Barcelona, Spain; [b]Department of Molecular Life Sciences, University of Zurich, CH-8057 Zurich, Switzerland; [c]Universitat Pompeu Fabra, 08002 Barcelona, Spain; [d]Medical Genetics, Department of Precision Medicine, University of Campania "L. Vanvitelli", 80138 Naples, Italy; [e]Telethon Institute of Genetics and Medicine, 80078 Pozzuoli, Italy; [f]Ecosustainable Marine Biotechnology Department, Stazione Zoologica Anton Dohrn, 80121 Naples, Italy; and [g]Institució Catalana de Recerca i Estudis Avançats, 08010 Barcelona, Spain

Author contributions: L.C., S.A.H., and M.I. designed research; L.C., F.M., L.L.-B., J.P., C.R.-M., J.Z., S.J.-D., S. Bonnal, and S.C. performed research; L.L.-B., J.P., C.R.-M., V.R., S.C.F.N., and S. Banfi contributed new reagents/analytic tools; L.C., F.M., J.Z., D.C., S.M.-V., S.C., S.A.H., and M.I. analyzed data; L.C., L.S., S.A.H., and M.I. wrote the paper; V.R., S.C.F.N., S. Banfi, L.S., S.A.H., and M.I. supervised research; and L.S., S.A.H., and M.I. supervised bioinformatic analyses.

1. K. J. Wert, J. H. Lin, S. H. Tsang, General pathophysiology in retinal degeneration. *Dev. Ophthalmol.* **53**, 33–43 (2014).
2. M. Hoon, H. Okawa, L. Della Santina, R. O. L. Wong, Functional architecture of the retina: Development and disease. *Prog. Retin. Eye Res.* **42**, 44–84 (2014).
3. L. J. Campbell, M. C. West, A. M. Jensen, A high content, small molecule screen identifies candidate molecular pathways that regulate rod photoreceptor outer segment renewal. *Sci. Rep.* **8**, 14017 (2018).
4. L. Sánchez-Bellver, V. Toulis, G. Marfany, On the wrong track: Alterations of ciliary transport in inherited retinal dystrophies. *Front. Cell Dev. Biol.* **9**, 623734 (2021).
5. A. M. Waters, P. L. Beales, Ciliopathies: An expanding disease spectrum. *Pediatr. Nephrol.* **26**, 1039–1056 (2011).
6. G. Wheway, J. Lord, D. Baralle, Splicing in the pathogenesis, diagnosis and treatment of ciliopathies. *Biochim. Biophys. Acta. Gene Regul. Mech.* **1862**, 194433 (2019).
7. D. Murphy, B. Cieply, R. Carstens, V. Ramamurthy, P. Stoilov, The Musashi 1 controls the splicing of photoreceptor-specific exons in the vertebrate retina. *PLoS Genet.* **12**, e1006256 (2016). Erratum in *PLos Genet.* **12**, e1006432 (2016).
8. J. P. Ling *et al.*, ASCOT identifies key regulators of neuronal subtype-specific splicing. *Nat. Commun.* **11**, 137 (2020).
9. M. M. Liu, D. J. Zack, Alternative splicing and retinal degeneration. *Clin. Genet.* **84**, 142–149 (2013).
10. M. Irimia *et al.*, A highly conserved program of neuronal microexons is misregulated in autistic brains. *Cell* **159**, 1511–1523 (2014).

11. Y. I. Li, L. Sanchez-Pulido, W. Haerty, C. P. Ponting, RBFOX and PTBP1 proteins regulate the alternative splicing of micro-exons in human brain transcripts. *Genome Res.* **25**, 1–13 (2015).
12. N. Volfovsky, B. J. Haas, S. L. Salzberg, Computational discovery of internal micro-exons. *Genome Res.* **13** (6A), 1216–1221 (2003).
13. J. D. Ellis *et al.*, Tissue-specific alternative splicing remodels protein-protein interaction networks. *Mol. Cell* **46**, 884–892 (2012).
14. A. Torres-Méndez *et al.*, A novel protein domain in an ancestral splicing factor drove the evolution of neural microexons. *Nat. Ecol. Evol.* **3**, 691–701 (2019).
15. J. Ule *et al.*, An RNA map predicting Nova-dependent splicing regulation. *Nature* **444**, 580–586 (2006).
16. C. Zhang *et al.*, Defining the regulatory network of the tissue-specific splicing factors Fox-1 and Fox-2. *Genes Dev.* **22**, 2550–2563 (2008).
17. J. A. Calarco *et al.*, Regulation of vertebrate nervous system alternative splicing and development by an SR-related protein. *Cell* **138**, 898–910 (2009).
18. M. Quesnel-Vallières *et al.*, Misregulation of an activity-dependent splicing network as a common mechanism underlying autism spectrum disorders. *Mol. Cell* **64**, 1023–1034 (2016).
19. M. Quesnel-Vallières, M. Irimia, S. P. Cordes, B. J. Blencowe, Essential roles for the splicing regulator nSR100/SRRM4 during nervous system development. *Genes Dev.* **29**, 746–759 (2015).
20. Y. Nakano *et al.*, A mutation in the Srrm4 gene causes alternative splicing defects and deafness in the Bronx waltzer mouse. *PLoS Genet.* **8**, e1002966 (2012).
21. Y. Nakano, S. Wiechert, B. Bánfi, Overlapping activities of two neuronal splicing factors switch the GABA effect from excitatory to inhibitory by regulating REST. *Cell Rep.* **27**, 860–871.e8 (2019).
22. T. Gonatopoulos-Pournatzis *et al.*, Autism-misregulated eIF4G microexons control synaptic translation and higher order cognitive functions. *Mol. Cell* **77**, 1176–1192.e16 (2020).
23. J. Tapial *et al.*, An atlas of alternative splicing profiles and functional associations reveals new regulatory programs and genes that simultaneously express multiple major isoforms. *Genome Res.* **27**, 1759–1768 (2017).
24. L. Li, M. Anand, K. N. Rao, H. Khanna, Cilia in photoreceptors. *Methods Cell Biol.* **127**, 75–92 (2015).
25. S. Kim *et al.*, Generation, transcriptome profiling, and functional validation of cone-rich human retinal organoids. *Proc. Natl. Acad. Sci. U.S.A.* **116**, 10824–10833 (2019).
26. S. Veleri *et al.*, Ciliopathy-associated gene Cc2d2a promotes assembly of subdistal appendages on the mother centriole during cilia biogenesis. *Nat. Commun.* **5**, 4207 (2014).
27. S. Roosing *et al.*; POC1B Study Group, Disruption of the basal body protein POC1B results in autosomal-recessive cone-rod dystrophy. *Am. J. Hum. Genet.* **95**, 131–142 (2014).
28. C. J. Wiens *et al.*, Bardet-Biedl syndrome-associated small GTPase ARL6 (BBS3) functions at or near the ciliary gate and modulates Wnt signaling. *J. Biol. Chem.* **285**, 16218–16230 (2010).
29. Z. Lu *et al.*, Deletion of the transmembrane protein Prom1b in zebrafish disrupts outer-segment morphogenesis and causes photoreceptor degeneration. *J. Biol. Chem.* **294**, 13953–13963 (2019).
30. A. Plana-Bonamaisó *et al.*, Post-translational regulation of retinal IMPDH1 in vivo to adjust GTP synthesis to illumination conditions. *eLife* **9**, e56418 (2020).
31. G. J. Pazour *et al.*, The intraflagellar transport protein, IFT88, is essential for vertebrate photoreceptor assembly and maintenance. *J. Cell Biol.* **157**, 103–113 (2002).
32. K. Nakayama, Y. Katoh, Ciliary protein trafficking mediated by IFT and BBSome complexes with the aid of kinesin-2 and dynein-2 motors. *J. Biochem.* **163**, 155–164 (2018).
33. A. Wiegering, U. Rüther, C. Gerhardt, The ciliary protein Rpgrip1l in development and disease. *Dev. Biol.* **442**, 60–68 (2018).
34. P. R. Pretorius *et al.*, Identification and functional analysis of the vision-specific BBS3 (ARL6) long isoform. *PLoS Genet.* **6**, e1000884 (2010).
35. A. Vig *et al.*; Genomics England Research Consortium, DYNC2H1 hypomorphic or retina-predominant variants cause nonsyndromic retinal degeneration. *Genet. Med.* **22**, 2041–2051 (2020).
36. J. Mistry *et al.*, Pfam: The protein families database in 2021. *Nucleic Acids Res.* **49**, D412–D419 (2021).
37. N. Hulo *et al.*, The PROSITE database. *Nucleic Acids Res.* **34**, D227–D230 (2006).
38. U. Pieper *et al.*, ModBase, a database of annotated comparative protein structure models and associated resources. *Nucleic Acids Res.* **42**, D336–D346 (2014).
39. R. Mosca, T. Pons, A. Céol, A. Valencia, P. Aloy, Towards a detailed atlas of protein-protein interactions. *Curr. Opin. Struct. Biol.* **23**, 929–940 (2013).
40. C. Savojardo, M. Manfredi, P. L. Martelli, R. Casadio, Solvent accessibility of residues undergoing pathogenic variations in humans: From protein structures to protein sequences. *Front. Mol. Biosci.* **7**, 626363 (2021).
41. E. ter Haar, S. C. Harrison, T. Kirchhausen, Peptide-in-groove interactions link target proteins to the β-propeller of clathrin. *Proc. Natl. Acad. Sci. U.S.A.* **97**, 1096–1100 (2000).
42. F. Buss, S. D. Arden, M. Lindsay, J. P. Luzio, J. Kendrick-Jones, Myosin VI isoform localized to clathrin-coated vesicles with a role in clathrin-mediated endocytosis. *EMBO J.* **20**, 3676–3684 (2001).
43. J. Ménétrey *et al.*, The structure of the myosin VI motor reveals the mechanism of directionality reversal. *Nature* **435**, 779–785 (2005).
44. S. Niekamp, N. Coudray, N. Zhang, R. D. Vale, G. Bhabha, Coupling of ATPase activity, microtubule binding, and mechanics in the dynein motor domain. *EMBO J.* **38**, e101414 (2019).
45. Y. Márquez *et al.*, ExOrthist: A tool to infer exon orthologies at any evolutionary distance. *Genome Biol.* **22**, 239.
46. S. A. Head *et al.*, Silencing of SRRM4 suppresses microexon inclusion and promotes tumor growth across cancers. *PLoS Biol.* **19**, e3001138 (2021).
47. J. T. Witten, J. Ule, Understanding splicing regulation through RNA splicing maps. *Trends Genet.* **27**, 89–97 (2011).
48. M. Matsushita, R. Yamamoto, K. Mitsui, H. Kanazawa, Altered motor activity of alternative splice variants of the mammalian kinesin-3 protein KIF1B. *Traffic* **10**, 1647–1654 (2009).
49. PLOS Genetics Staff, Correction: The Musashi 1 controls the splicing of photoreceptor-specific exons in the vertebrate retina. *PLoS Genet.* **12**, e1006432 (2016).
50. S. M. Weyn-Vanhentenryck *et al.*, Precise temporal regulation of alternative splicing during neural development. *Nat. Commun.* **9**, 2189 (2018).
51. G. Stearns, M. Evangelista, J. M. Fadool, S. E. Brockerhoff, A mutation in the cone-specific pde6 gene causes rapid cone photoreceptor degeneration in zebrafish. *J. Neurosci.* **27**, 13866–13874 (2007).
52. S. Hochmann *et al.*, Fgf signaling is required for photoreceptor maintenance in the adult zebrafish retina. *PLoS One* **7**, e30365 (2012).
53. S. Mirra, G. Marfany, Mitochondrial gymnastics in retinal cells: A resilience mechanism against oxidative stress and neurodegeneration. *Adv. Exp. Med. Biol.* **1185**, 513–517 (2019).
54. S. Mirra *et al.*, CERKL, a retinal dystrophy gene, regulates mitochondrial function and dynamics in the mammalian retina. *Neurobiol. Dis.* **156**, 105405 (2021).
55. W. J. Spencer *et al.*, PRCD is essential for high-fidelity photoreceptor disc formation. *Proc. Natl. Acad. Sci. U.S.A.* **116**, 13087–13096 (2019).
56. S. Sukumaran, B. D. Perkins, Early defects in photoreceptor outer segment morphogenesis in zebrafish ift57, ift88 and ift172 intraflagellar transport mutants. *Vision Res.* **49**, 479–489 (2009).
57. I. Ojeda Naharros *et al.*, Loss-of-function of the ciliopathy protein Cc2d2a disorganizes the vesicle fusion machinery at the periciliary membrane and indirectly affects Rab8-trafficking in zebrafish photoreceptors. *PLoS Genet.* **13**, e1007150 (2017).
58. Y. V. Makhankov, O. Rinner, S. C. F. Neuhauss, An inexpensive device for non-invasive electroretinography in small aquatic vertebrates. *J. Neurosci. Methods* **135**, 205–210 (2004).
59. J. Bilotta, S. Saszik, S. E. Sutherland, Rod contributions to the electroretinogram of the dark-adapted developing zebrafish. *Dev. Dyn.* **222**, 564–570 (2001).
60. C. Crespo, E. Knust, Characterisation of maturation of photoreceptor cell subtypes during zebrafish retinal development. *Biol. Open* **7**, bio036632 (2018).
61. M. Tsujikawa, J. Malicki, Intraflagellar transport genes are essential for differentiation and survival of vertebrate sensory neurons. *Neuron* **42**, 703–716 (2004).
62. C. Insinna, L. M. Baye, A. Amsterdam, J. C. Besharse, B. A. Link, Analysis of a zebrafish dync1h1 mutant reveals multiple functions for cytoplasmic dynein 1 during retinal photoreceptor development. *Neural Dev.* **5**, 12 (2010).
63. S. van Soest, A. Westerveld, P. T. de Jong, E. M. Bleeker-Wagemakers, A. A. Bergen, Retinitis pigmentosa: Defined from a molecular point of view. *Surv. Ophthalmol.* **43**, 321–334 (1999).
64. G. Martín, Y. Márquez, F. Mantica, P. Duque, M. Irimia, Alternative splicing landscapes in *Arabidopsis thaliana* across tissues and stress conditions highlight major functional differences with animals. *Genome Biol.* **22**, 35 (2021).
65. A. Gohr, M. Irimia, Matt: Unix tools for alternative splicing analysis. *Bioinformatics* **35**, 130–132 (2019).
66. J. Letelier *et al.*, Mutation of Vsx genes in zebrafish highlights the robustness of the retinal specification network. *bioRxiv* [Preprint] (2022). https://www.biorxiv.org/content/10.1101/2022.01.20.477122v1.
67. J. Zang, J. Keim, E. Kastenhuber, M. Gesemann, S. C. F. Neuhauss, Recoverin depletion accelerates cone photoresponse recovery. *Open Biol.* **5**, 150086 (2015).
68. O. Rinner, J. M. Rick, S. C. F. Neuhauss, Contrast sensitivity, spatial and temporal tuning of the larval zebrafish optokinetic response. *Invest. Ophthalmol. Vis. Sci.* **46**, 137–142 (2005).
69. L. Ciampi, S. Head, L. Serrano, and M.I Irimia, Regulation of retina microexons. GEO Data Base. https://www.ncbi.nlm.nih.gov/geo/query/acc.cgi?&acc=GSE180781. Deposited 14 April 2022.